

Short Communication

In-situ Fabrication of Ru/C₃N₄ Nanosheets Mott-Schottky Photocatalyst for Enhanced Photocatalytic H₂ Evolution

Jiangqi Ning, Youhua Chen, Ting Wang, Jinhua Xiong*

Fujian Provincial Key Laboratory of Clean Energy Materials, Longyan University, Longyan 364000, P. R. China.

*E-mail: xjh970996937@sina.com

Received: 1 May 2022 / Accepted: 13 June 2022 / Published: 4 July 2022

Herein, we developed a strategy for preparing Ru/C₃N₄ nanosheets with mott-schottky junction, denoted as C₃N₄-Ru-x. Tris(2,2-bipyridyl)ruthenium(II) chloride hexahydrate (Ru(bpy)₃Cl₂) was used as a catalyst to promote the thermal exfoliation of bulk g-C₃N₄ under 680 °C for 5 min in air. As a consequence, g-C₃N₄ nanosheets with mesoporous were formed and metal Ru was in-situ anchored on g-C₃N₄ nanosheets. X-ray diffraction verified the effect of the Ru(bpy)₃Cl₂ on promoting exfoliation of bulk g-C₃N₄. TEM directly demonstrated g-C₃N₄ nanosheets with mesoporous were formed and the metal Ru was about 2.5 nm. XPS confirmed the formation of a schottky junction between Ru and g-C₃N₄ nanosheets. The sample of C₃N₄-Ru-2.0 with a loading amount of Ru (0.52%) showed a photocatalytic H₂ production activity of 42.8 μmol/h. The linear sweep voltammetry (LSV) curve and electrochemical impedance spectroscopy (EIS) showed C₃N₄-Ru-2.0 had a lower hydrogen evolution overpotential and a smaller charge transfer resistance than C₃N₄-Ru-0, verifying the promotion effect of Ru on hydrogen evolution of C₃N₄ nanosheets.

Keywords: charge carriers separation and transfer, H₂, mott-schottky junction, C₃N₄ nanosheets, Ru

1. INTRODUCTION

For achieving a sustainable developing society, a green and high-energy energy is in demand. Hydrogen is considered to be an ideal energy for resolving this issue. Photocatalytic hydrogen production as a clean and powerful technology has arisen extensive attraction [1]. Photocatalysis strongly depends on the structure, components, morphology, et al. of photocatalysts. Search and rational design of a photocatalyst has been a key route to obtain a photocatalyst with a high reaction efficiency.

Among hydrogen evolution photocatalysts, graphitic carbon nitride (g-C₃N₄) stands out because of its easy obtainment, tunable energy band and chemical structure, various morphologies,

facile post-modification, thermodynamic stability, et al [2]. g-C₃N₄ is generally synthesized via a simple thermal polymerization of some organic substances including C and N elements, such as urea, melamine, dicyandiamide, et al [3]. g-C₃N₄ is used to considered as a polymer semiconductor with a band gap of 2.7 eV, a conduction band and a valence band located at about -1.3 eV and 1.4 eV (vs. NHE, pH=7), respectively. The energy structure endows g-C₃N₄ with a capacity for overall splitting of H₂O. Moreover, the energy band of g-C₃N₄ can be adjusted via diverse strategies including protonation [4], doping [5], exfoliation [6], matrix of g-C₃N₄ modification [7]. While, a fatal drawback affected photocatalytic hydrogen evolution activity of g-C₃N₄ is the poor separation efficiency of carriers and the low active sites. To solve these problems, improving the electrical conductivity and surface areas of g-C₃N₄ via loading metal and designing structure, respectively, has been an universal route [8, 9]. However, although loading metal, such as Pt, Pd, Ru, Au, Ir, et al., can improve the electrical conductivity of g-C₃N₄ and facilitate lowering the hydrogen evolution potential, metal might be easy to fall off g-C₃N₄, if the metals were deposited on g-C₃N₄ surface via post-loading method, for example loading of Pt via impregnation and reduction by NaBH₄. As for improving surface areas, designing g-C₃N₄ with mesoporous or ultrathin nanosheets structure has been proved to meet this demand [10, 11]. As reported, mesoporous g-C₃N₄ synthesized via hard or soft template exhibits remarkably increasing surface areas [12]. However, the use of template generally need tedious procedures to synthesize and remove the template. Therefore, g-C₃N₄ nanosheets obtained from liquid exfoliation or thermal exfoliation show advantages in the application of photocatalysis due to the unique structure features, such as large surface area, flexibility and short carrier migration path [13, 14]. Hence, increasing the surface area of g-C₃N₄ and achieving metal as the cocatalyst anchored on g-C₃N₄ simultaneously will facilitate the photocatalysis of g-C₃N₄.

Herein, we developed a strategy for preparing photocatalyst with highly dispersed Ru about 2.5 nm anchored on C₃N₄ nanosheets, denoted as C₃N₄-Ru-x. Tris(2,2-bipyridyl)ruthenium(II) chloride hexahydrate (Ru(bpy)₃Cl₂) was used as a catalyst to promote the thermal exfoliation of bulk g-C₃N₄. As a consequence, g-C₃N₄ nanosheets with mesoporous were formed and metal Ru was in-situ anchored on g-C₃N₄ nanosheets. The as-prepared C₃N₄-Ru-x showed an excellent photocatalytic H₂ production activity because of the large surface area and schottky junction formed between Ru and g-C₃N₄ nanosheets.

2. EXPERIMENT SECTION

2.1. Materials for preparing photocatalysts

Melamine, Tris(2,2-bipyridyl)ruthenium(II) chloride hexahydrate (Ru(bpy)₃Cl₂•6H₂O), H₂PtCl₆•6H₂O, ethanol, triethanolamine, home-made deionized water. All materials were analytic reagents.

2.2. Preparation of photocatalyst

Preparation of bulk C_3N_4 (B- C_3N_4). Melamine (10 g) was ground into powder and calcined at 550 °C for 2h in air (with a ramping rate of 4.0 °C/min). The obtained B- C_3N_4 was ground into powder.

Preparation of Ru nanoparticles decorated porous C_3N_4 nanosheets (C_3N_4 -Ru-x, x is the percentage amount of $Ru(bpy)_3Cl_2 \cdot 6H_2O$ in the mixture before calcination). 1.0 g B- C_3N_4 and 2 mL ethanol contained different amount of $Ru(bpy)_3Cl_2 \cdot 6H_2O$ (0 mg, 5 mg, 10 mg 20 mg, respectively) were mixed and ground until dry. Then, the sample was rapidly put into a muffle furnace with a temperature of 680 °C for 5 minutes and taken out immediately. The as-prepared samples with various amount of $Ru(bpy)_3Cl_2 \cdot 6H_2O$ were denoted as C_3N_4 -Ru-0, C_3N_4 -Ru-0.5%, C_3N_4 -Ru-1.0% and C_3N_4 -Ru-2.0%, respectively.

2.3. Characterization

X-ray diffraction (XRD) dates were obtained by using Powder X-ray diffractometer (X'Pert3, Cu Ka radiation, 40 kV and 40 mA). The transmission electron microscopy (TEM) images and high-resolution (HR) TEM images were obtained on a equipment of Talos F200S. X-ray photoelectron spectroscopy (XPS) dates were recorded on a equipment of ThermoScientific K-Alpha. Binding energy dates were calibrated with the reference of $C_{1s}=284.8$ eV. Ultraviolet-visible absorption (UV-vis Abs) spectra were recorded on UV-2600, $BaSO_4$ as the reference. The Brunauer–Emmett–Teller (BET) surface area was measured with an TriStar II Plus apparatus (Micromeritics Instrument Corp). Inductive couple plasma atomic emission spectrometry (ICP-AES) perofrmed on Agilent 5110 was used to decided the amount of Ru in photocatalyst. Fourier transform infrared (FTIR) spectra of the samples were performed on a Nicolet Nexus 670 FTIR spectrometer at a resolution of 4 cm^{-1} . Electrochemical measurements were carried out on an electrochemical station (CHI660E) with a three-electrode system. A platinum wire and a saturated calomel electrode (SCE) were used as counter electrode and reference electrode, respectively. Glassy carbon (GC) disk electrode with a diameter of 3 mm was used as a working electrode. Ethanol and deionized water were used to clean the GC electrode before using. To obtain the sample ink, 5 mg sample powder was dispersed well in a mixed solution including 600 μL ethanol, 300 μL deionized water and 100 μL 40% nafion aqueous solution under ultrasonication. 10 μL sample ink was spreaded on GC disk. After air drying naturally, the electrodes were suffered from a heat treatment at 60 °C for 2 h in vacuum environment. Linear sweep voltammetry (LSV) and electrochemical impedance spectroscopy (EIS) tests were performed in 0.2 M Na_2SO_4 aqueous solution with 10 % v/v triethanolamine under argon atmosphere. Scan rate of LSV was 25 $mV s^{-1}$ and the EIS was carried out in a frequency range of 10^{-1} to 10^5 Hz with a 5 mV amplitude.

2.4. photocatalytic tests.

The photocatalytic hydrogen evolution reactions were performed on MC-H20II, a Pyrex reaction system equipped a closed gas circulation and evacuation system. 40 mg as-prepared sample

was dispersed in 50 mL 10 % v/v triethanolamine aqueous solution. The suspension was degassed well and then irradiated by light ($\lambda > 400$ nm) with a Xenon lamp (300 W, PLS-SXE300D). H_2 was quantified by an online gas chromatograph.

3. RESULT AND DISCUSSION

3.1 structure and light absorption property

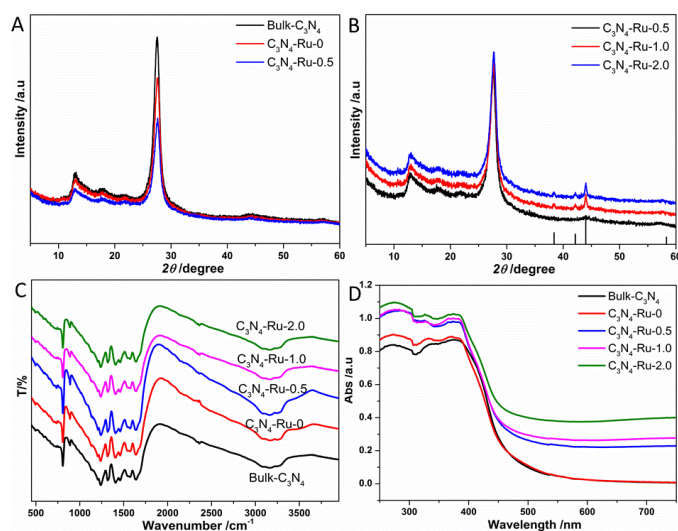


Figure 1. A-B) XRD diffraction patterns, C) FTIR and D) UV-vis Abs spectra of B-C₃N₄ and C₃N₄-Ru-x (x=0, 0.5, 1.0 and 2.0) respectively.

XRD diffraction patterns of the as-prepared samples were shown in Fig. 1A and 1B. As shown, the bulk C₃N₄ (B-C₃N₄) showed two distinct peaks at 12.7° and 27.7°, corresponding to the diffraction plane of the in-plane structural repeating units of tri-s-triazine and the graphite-like stacking plane of (002), respectively [15]. Furthermore, the XRD diffraction patterns of C₃N₄-Ru-0 and C₃N₄-Ru-0.5 were similar with that of B-C₃N₄, demonstrating the samples sustained the structure of C₃N₄. While, compared with B-C₃N₄, C₃N₄-Ru-0 and C₃N₄-Ru-0.5 had a lower intensity at 27.7°, which arose from a thermal exfoliation effect that resulted in a low crystallinity in c direction [6, 13]. A weaker intensity of C₃N₄-Ru-0.5 than that of C₃N₄-Ru-0, meaning that the added Ru(bpy)₃Cl₂ promoted the exfoliation of C₃N₄. While, as shown in Fig. 1B, along with the increase content of Ru(bpy)₃Cl₂, the XRD diffraction patterns corresponding to the C₃N₄ showed no distinct change, but the counterpart assigned to metal Ru⁰ occurred. The three obvious diffraction peaks at 38.4°, 42.5° and 44.8° were ascribed to (100), (002) and (101) planes of metal Ru⁰, respectively, matching well with the referenced dates (PDF#06-0663) [16, 17]. Moreover, the FTIR spectra of B-C₃N₄ and C₃N₄-Ru-x (x=0, 0.5, 1.0 and 2.0) showed characteristic absorption peaks corresponding to the chemical structure of C₃N₄. The sharp peak at 807 cm⁻¹ was assigned to the breathing vibration of s-triazine ring system. The finger peaks located at 1200-1750 cm⁻¹ belonged to the aromatic CN heterocycles [13]. The broad peaks between 3400 and 3000 cm⁻¹ were originated from the N-H and/or NH₂ groups, which are integral parts of melon. Additionally, the UV-vis Abs spectra (Fig. 1D) demonstrated the absorption spectra of all the samples were analogous, having an adsorption edge (λ_{abs}) around 450 nm. Moreover, the bandgap (E_g)

of C_3N_4 was estimated to be 2.75 eV via $E_g \approx 1240/\lambda_{abs}$ [18, 19]. Additionally, Ru-modified samples possessed an enhanced absorptions in the range of 450-750 nm, when compared with the C_3N_4 -Ru-0. Furthermore, the absorption intensity enhanced along with increasing content of Ru^0 . The increasing absorption should result from the light scattering effect of the Ru^0 nanoparticles on C_3N_4 [20].

3.2. Morphology and specific surface areas

Fig. 2A-C showed the morphologies of B- C_3N_4 and C_3N_4 -Ru-0 and C_3N_4 -Ru-2.0, respectively. As shown, B- C_3N_4 was a kind of brick-like bulked material. C_3N_4 -Ru-0 somewhat sustained the blocky structure, but lots of fragment appeared on surface. While, C_3N_4 -Ru-2.0 was loose and porous agglomerates stacked by nanosheets. The changes of the morphologies directly confirmed C_3N_4 suffered from the thermal exfoliation.

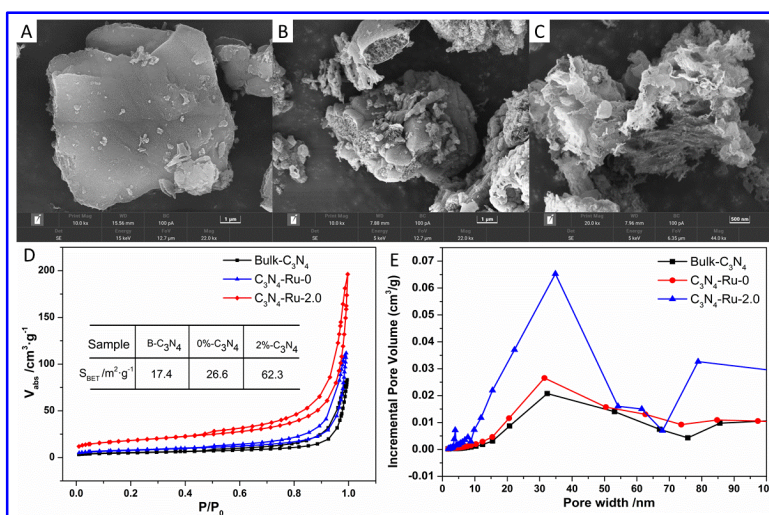


Figure 2. A-C) SEM images, D-E) BET adsorption at different P/P_0 and pore size distribution curves for B- C_3N_4 and C_3N_4 -Ru-0 and C_3N_4 -Ru-2.0, respectively.

Moreover, BET N_2 adsorption-desorption isothermal measurements were performed for evaluating the specific surface areas and pore size distributions of the samples (Fig. 2D). As shown, C_3N_4 -Ru-2.0 had a BET surface of $62.3 \text{ m}^2/\text{g}$, much higher than that of C_3N_4 -Ru-0 ($26.6 \text{ m}^2/\text{g}$) and B- C_3N_4 ($17.4 \text{ m}^2/\text{g}$), which benefited for increasing surface active sites. Moreover, the isotherm of these samples showed a typical hysteresis, demonstrating the samples had mesopores [9]. Pore size distribution curve (Fig. 2E) demonstrated the pore size centered at 10-50 nm. Additionally, as compared with C_3N_4 -Ru-0 and B- C_3N_4 , C_3N_4 -Ru-2.0 had an obviously enhanced pore volume, indicating that the increased BET surface resulted from the occurrence of pore [21]. Additionally, TEM was used to further verify the pores existed in C_3N_4 -Ru-2.0. Fig. 3A-C demonstrated C_3N_4 -Ru-2.0 was assembled by C_3N_4 nanosheets with many mesoporous. Additionally, as shown in Fig. 3B and C, many nanoparticles with a size around 2.5 nm dispersed well on C_3N_4 nanosheets. The nanoparticle had a distinct lattice fringes with a spacing distance of 0.208 nm corresponding to the (101) plane of

metal Ru, further demonstrating $\text{Ru}(\text{bpy})_3\text{Cl}_2$ was transformed into Ru after thermal treatment, which matched the result of XRD. The actual content of Ru in $\text{C}_3\text{N}_4\text{-Ru-2.0}$ was 0.52 % decided by ICP-AES. Moreover, the formation of Ru^0 should arise from the reduction effect of NO, $(\text{CN})_2$ or someone reducing gas generated via decomposition of C_3N_4 [22].

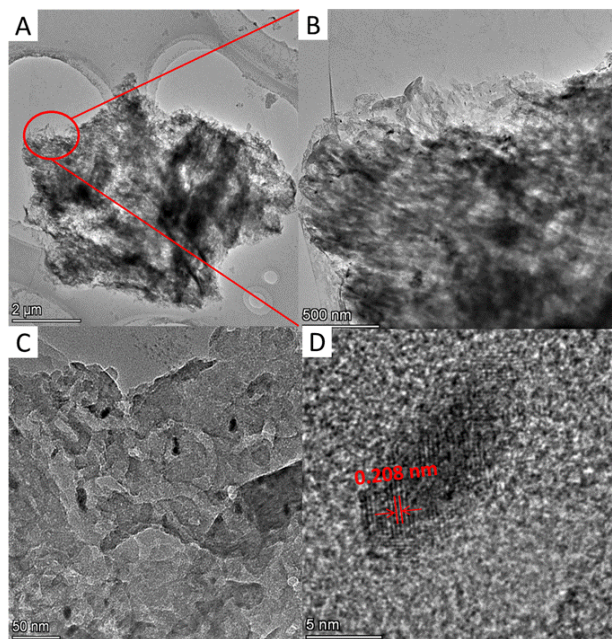


Figure 3. A-C) TEM images in various resolutions and D) HRTEM images of $\text{C}_3\text{N}_4\text{-Ru-2.0}$

3.3 XPS analysis and activity

For making clear the chemical oxidation state of the elements in $\text{C}_3\text{N}_4\text{-Ru-x}$, XPS was used to analyze the samples. Fig. 4A demonstrated the survey spectra of $\text{C}_3\text{N}_4\text{-Ru-0}$ and $\text{C}_3\text{N}_4\text{-Ru-2.0}$ had three obvious peaks assigned to elements of O 1s, C 1s and N 1s. The occurrence of the oxygen was due to the surface absorbed oxygen species [13]. For $\text{C}_3\text{N}_4\text{-Ru-2.0}$, an additional tiny peak at around 460 eV was attributed to Ru 3p. Additionally, both samples showed typical binding states for fine spectra of C 1s and N 1s in C_3N_4 . As shown in Fig. 4B, $\text{C}_3\text{N}_4\text{-Ru-0}$ and $\text{C}_3\text{N}_4\text{-Ru-2.0}$ had a very similar C 1s spectra deconvoluted into three peaks at binding energy of 284.8, 286.4 and 288.2 eV, which was assigned to referenced carbon, C-NH₂ and C(N)₃ existed in the framework of C_3N_4 , respectively [7, 22]. For $\text{C}_3\text{N}_4\text{-Ru-2.0}$, the N 1s spectrum was fitted into four peaks at binding energies of 398.7, 400.1, 401.2 and 404.3 eV, respectively, corresponding to the sp²-bonded N (C-N=C) in the triazine rings, the tertiary nitrogen N-(C)₃, the amino functions (C-N-H) and the π-excitations, respectively [7, 22]. The binding energies of N 1s corresponding to different N in $\text{C}_3\text{N}_4\text{-Ru-2.0}$ had a shift of 0.1-0.3 eV towards higher binding energy, when compared with those in $\text{C}_3\text{N}_4\text{-Ru-0}$. These shifts arose from the generation of schottky junction between Ru^0 and C_3N_4 , leading to a charge density transfer from C_3N_4 to Ru^0 [21]. As well known, a schottky junction between metal and semiconductor facilitated a separation of photo-generated carriers, thus resulting in an enhanced photocatalytic activity [23]. Finally, the existence of Ru^0 on C_3N_4 was further evidenced by Ru 3p spectrum. As shown in Fig. 4D,

the Ru 3p sepectrum of C₃N₄-Ru-2.0 showed two weak peaks at binding energies of 462.1 and 484.6 eV, corresponding to 3p_{3/2} and 3p_{1/2} of Ru⁰ [17, 24].

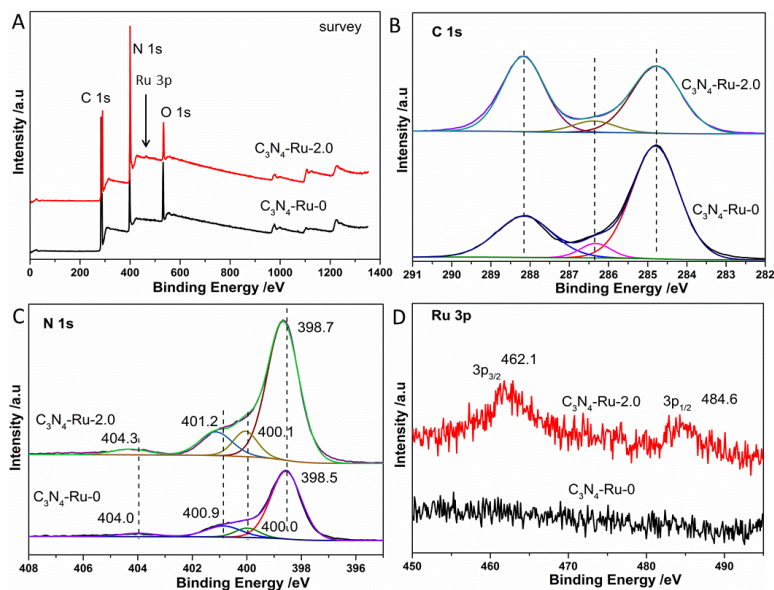


Figure 4. XPS analysis for C₃N₄-Ru-0 and C₃N₄-Ru-2.0, A) survey, B) C 1s, C) N 1s and D) Ru 3p.

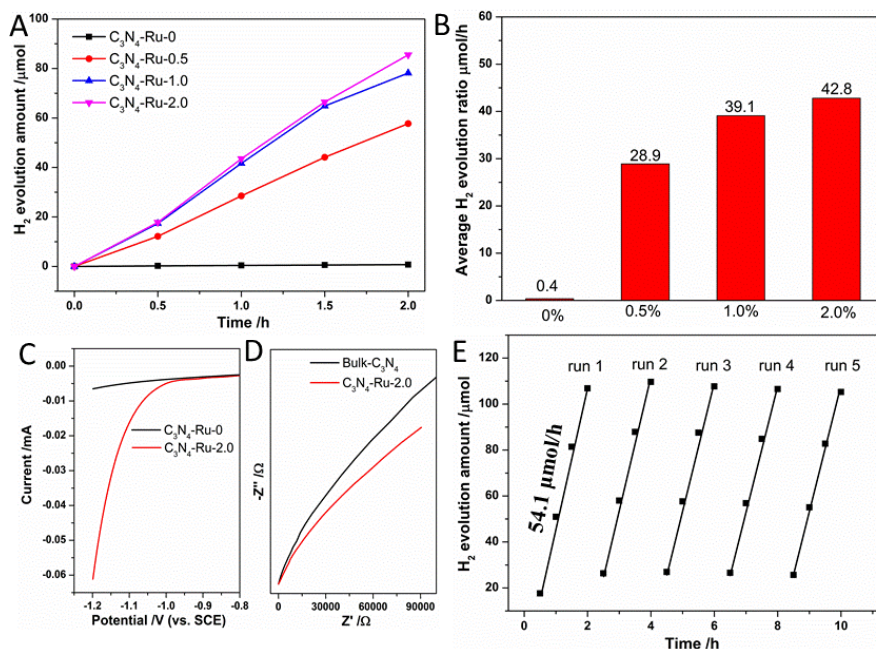


Figure 5. A-B) curves of H₂ production versus time and the corresponding H₂ evolution rates over the C₃N₄-Ru-x (x=0, 0.5, 1.0 and 2.0), respectively; C-D) Linear sweep voltammetry curves and electrochemical impedance spectroscopy of C₃N₄-Ru-0 and C₃N₄-Ru-2.0, respectively; E) photocatalytic H₂ evolution activity in 5 runs for C₃N₄-Ru-2.0 with in-situ adding of 1% Pt.

As shown in Fig. 5A, C₃N₄-Ru-0 showed no obvious photocatalytic H₂ evolution activity. After loading with Ru, C₃N₄-Ru-x (x=0.5, 1.0 and 2.0) exhibited a sharply increasing photocatalytic H₂ evolution activity, which arose from the promotion effect of Ru as a H₂ evolution cocatalysts. Fig. 5B showed the average H₂ production rates for C₃N₄-Ru-x (x=0, 0.5, 1.0 and 2.0) were 0.4, 28.9, 39.1 and 42.8 μmol h⁻¹ (1070 μmol • g⁻¹ • h⁻¹), respectively. As shown in Table 1, the photocatalytic H₂ evolution activity of C₃N₄-Ru-x in this work was at middle level, as compared with that of other Ru-modified C₃N₄ photocatalysts reported in recent years [25-30]. Additionally, as shown in Fig. 5C and 5D, Linear sweep voltammetry curves and electrochemical impedance spectroscopy (EIS) demonstrated C₃N₄-Ru-2.0 had a lower overpotential and a smaller charge transfer resistance for H₂ evolution than bare C₃N₄-Ru-0, further verifying the promotion effect of Ru on C₃N₄ nanosheets for H₂ evolution [24]. Moreover, the photocatalytic activity of C₃N₄-Ru-2.0 was able to be adjusted via in-situ add of Pt. As shown in Fig. 5E, with add of 1% Pt, the average H₂ evolution rates of C₃N₄-Ru-2.0 increased to 54.1 μmol h⁻¹ and C₃N₄-Ru-2.0 showed an excellent stability in five runs for photocatalytic H₂ evolution.

Table 1. Comparison of the photocatalytic H₂ evolution activities of Ru modified C₃N₄

Photocatalyst	Sacrificial agent	H ₂ evolution activity /μmol • g ⁻¹ • h ⁻¹	Light/nm	Reference
C ₃ N ₄ /Ru	10% triethanolamine aqueous solution (10% TEOA)	1070	λ >400	This work
g-C ₃ N ₄ /Ru-NP	10% TEOA	394.3	λ >300	25
C ₃ N ₄ -Ru	10% TEOA	4052.1	λ >300	25
P-C ₃ N ₄ /Ru _x P	10% TEOA	1940	λ >300	26
C ₃ N ₄ /Ru	10% TEOA	1420	λ >300	26
P-C ₃ N ₄ /Ru	10% TEOA	1310	λ >300	26
C ₃ N ₄ /Ru-Pt	15% TEOA	887	λ >420	27
C ₃ N ₄ /Ru-CoP	10% TEOA	1172.5	λ >400	28
C ₃ N ₄ /Ru	5% CH ₃ OH aqueous solution	3160	λ >300	29
C ₃ N ₄ /Ru _x P	10% TEOA	2110	λ >420	30

4. CONCLUSION

we have developed a strategy for preparing Ru/C₃N₄ nanosheets with mott-schottky junction via thermal exfoliation of bulk g-C₃N₄ with Ru(bpy)₃Cl₂ as a catalyst under 680 °C for 5 min in air.

Metal Ru⁰ was in-situ anchored on g-C₃N₄ nanosheets and a schottky junction formed between Ru⁰ and g-C₃N₄ nanosheets. The sample of C₃N₄-Ru-2.0 with an optimal loading amount of Ru (0.52 %, wt) showed photocatalytic hydrogen evolution activity of 42.8 μmol h⁻¹. LSV and EIS experiments demonstrated a promotion effect of Ru on hydrogen evolution activity of C₃N₄ nanosheets, resulting from a lower hydrogen evolution overpotential and a smaller charge transfer resistance.

ACKNOWLEDGEMENTS

This work was supported by National Training Programs of Innovation and Entrepreneurship for Undergraduates (202111312001).

References

1. J. Xiong, Y. Li, S. Lu, W. Guo, J. Zou and Z. Fang, *Chem. Commun.*, 57 (2021) 8186.
2. Y. Wang, X. Wang and M. Antonietti, *Angew. Chem. Int. Ed.*, 51 (2012) 68.
3. J. Zhang, Y. Chen and X. Wang, *Energy Environ. Sci.*, 8 (2015) 3092.
4. Y. Zhang, A. Thomas, M. Antonietti and X. Wang, *J. Am. Chem. Soc.*, 131 (2009) 50.
5. G. Zhang, M. Zhang, X. Ye, X. Qiu, S. Lin and X. Wang, *Adv. Mater.*, 26 (2014) 805.
6. J. Xu, L. Zhang, R. Shi and Y. Zhu, *J. Mater. Chem. A*, 1 (2013) 14766.
7. M. Zhang and X. Wang, *Energy Environ. Sci.*, 7 (2014) 1902.
8. Q. Zhu, Z. Xu, B. Qiu, M. Xing and J. Zhang, *Small*, 17 (2021) 2101070.
9. J. Zhang, M. Zhang, C. Yang and X. Wang, *Adv. Mater.*, 26 (2014) 4121.
10. Y. Gong, M. Li and Y. Wang, *ChemSusChem*, 8 (2015) 931.
11. Y. Zheng, L. Lin, B. Wang and X. Wang, *Angew. Chem. Int. Ed.*, 54 (2015) 12868.
12. J. Xu, Y. Wang and Y. Zhu, *Langmuir*, 29 (2013) 10566.
13. Q. Lin, L. Li, S. Liang, M. Liu, J. Bi and L. Wu, *Appl. Catal. B: Environ.*, 163 (2015) 135.
14. P. Niu, L. Zhang, G. Liu and H.-M. Cheng, *Adv. Funct. Mater.*, 22 (2012) 4763.
15. P. Sharma and Y. Sasson, *Green Chem.*, 19 (2017) 844.
16. J. Peng, Y. Chen, K. Wang, Z. Tang and S. Chen, *Int. J. Hydrogen Energ.*, 45 (2020) 18840.
17. Q. Yao, B. Huang, N. Zhang, M. Sun, Q. Shao and X. Huang, *Angew. Chem. Int. Ed.*, 58 (2019) 13983.
18. J. Xiong, L. Wen, F. Jiang, Y. Liu, S. Liang and L. Wu, *J. Mater. Chem. A*, 3 (2015) 20627.
19. J. Xiong, K. Jing, J. Zou, S. Liang and L. Wu, *Dalton Trans.*, 46 (2017) 13935.
20. X. Han, T. Si, Q. Liu, F. Zhu, R. Li, X. Chen, J. Liu, H. Sun, J. Zhao, H. Ling, Q. Zhang and H. Wang, *Chem. Eng. J.*, 426 (2021) 130824.
21. S. Wang, D. Guo, M. Zong, C. Fan, X. Jun and D.-H. Wang, *Appl. Catal. A: Gen.*, 617 (2021) 118112.
22. P. Niu, M. Qiao, Y. Li, L. Huang and T. Zhai, *Nano Energy*, 44 (2018) 73.
23. Y. Shiraishi, Y. Kofuji, S. Kanazawa, H. Sakamoto, S. Ichikawa, S. Tanaka and T. Hirai, *Chem. Commun.*, 50 (2014) 15255.
24. J. Liu, G. Ding, J. Yu, X. Liu, X. Zhang, J. Guo, J. Zhang, W. Ren and R. Che, *J. Mater. Chem. A*, 7 (2019) 18072.
25. C. Li, X. Dong, Y. Zhang, J. Hu, J. Yuan, G. Li, D. Chen and Y. Li, *Appl. Surf. Sci.*, 596 (2022) 153471.
26. J. Zhang, Q. Zhu, Y. Ma, L. Wang, M. Nasir and J. Zhang, *Catal. Today*, 380 (2021) 223.
27. K. Mori, R. Osaka, K. Naka, D. Tatsumi and H. Yamashita, *ChemCatChem*, 11 (2019) 1963.
28. S. Meng, P. An, L. Chen, S. Sun, Z. Xie, M. Chen and D. Jiang, *J. Colloid. Interf. Sci.*, 585 (2021) 108.

29. B. Tahir, M. Tahir, M. Nawawai, A. Khoja, B. Haq and W. Farooq, *Int. J. Hydrogen Energ.*, 46 (2021) 27997.

30. J. Wang, J. Chen, P. Wang, J. Hou, C. Wang and Y. Ao, *Appl. Catal. B: Environ.*, 239 (2018) 578.

© 2022 The Authors. Published by ESG (www.electrochemsci.org). This article is an open access article distributed under the terms and conditions of the Creative Commons Attribution license (<http://creativecommons.org/licenses/by/4.0/>).